UNSTEADY VISCOELASTIC FLOW PAST A CYLINDER IN A CHANNEL

Paulo J. Oliveira
Depart. Eng. Electromecânica, Unidade de Materiais Têxteis e Papeleiros, Universidade da Beira Interior, 6200-001 Covilhã, Portugal
e-mail: pjpo@ubi.pt

Amílcar I. P. Miranda
Departamento de Matemática, Universidade da Beira Interior, 6201-001 Covilhã, Portugal.
e-mail: amiranda@noe.ubi.pt

Abstract. *In the present article we consider a rheological model with finite extensibility (the FENE-CR model) to simulate the flow around a confined cylinder placed symmetrically in a planar channel .Numerical problems related with infinite extensional viscosities are circumvented and higher levels of elasticity can be reached compared with previous work. With the usual assumption of symmetry about the centreline and by employing only half of the flow domain, we give results for the drag coefficient for Deborah numbers up to 10. When the full cylinder is considered, without calling for symmetry about the channel centreline, we show that the inertialess flow becomes unsteady and periodic at $De \approx 1.3$, with a separation bubble behind the cylinder.*

Keywords*. Viscoelastic FENE-CR, Cylinder, Numerical simulations, Finite volume method*

1. Introduction

One of the well-known benchmark flows in computational rheology is the confined flow past a cylinder placed symmetrically in a planar channel (Brown and McKinley, 1994). This configuration (Fig. 1) avoids the problems inherent to existence of geometrical singularities, as it is the case for flow through contractions, but still presents a number of challenges: thin stress boundary layers develop along the cylinder walls; co-existence of zones having predominant shear flow characteristics with zones of extensional flow type; formation of a thin stress wake behind the cylinder (bi-refringent strand).

In past work with this geometry (Alves et al. 2001), we have considered viscoelastic fluids which obeyed the quasi-linear constitutive models designated as the Upper-Convected Maxwell (UCM) model, and the Oldroyd-B model. The computations could be pursued up to Deborah numbers (De) of the order of unity yielding steady state solutions. For higher values of elasticity, as measured by the Deborah number, steady solutions could not be obtained. In the present work we consider a rheological model with finite extensibility, the FENE-CR model, so that numerical problems related with infinite extensional viscosities are circumvented and higher levels of elasticity can be reached. For the symmetrical geometry, we give results for the drag coefficient for Deborah numbers up to 10. When the full cylinder is considered, without calling for symmetry about the channel centreline, we show that the flow becomes unsteady and periodic at a Deborah number of about 1.3, with a small separation bubble behind the cylinder.
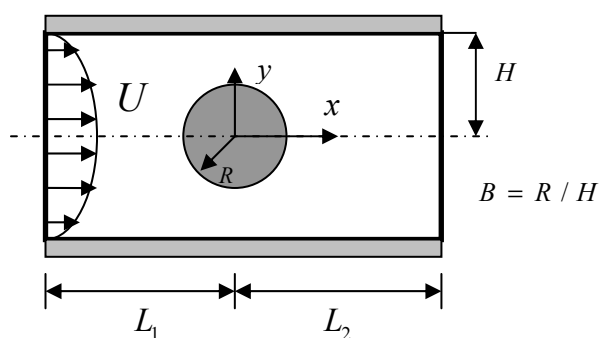

Figure 1 – Flow geometry.

Many of the earlier works dealing with viscoelastic flow around a cylinder (Liu et al., 1998; Fan et al., 1999; Sun et al., 1999; Dou and Phan-Thien, 1999; Alves et al., 2001) have employed either the UCM or the Oldroyd-B models to represent the rheology of the fluids. In the case of the latter model, it has been common to choose the solvent viscosity ratio as $\beta = \eta_s / \eta_0 = 0.59$, where η_0 is the zero-shear-rate viscosity given as the sum of solvent and "polymeric" contributions, $\eta_0 = \eta_s + \eta_p$. That particular value was based on the measured data for the MIT Boger fluid (McKinley et al., 1993), a solution of polyisobutylene dissolved in a polybutene and tetradecane mixture. The most accurate numerical solutions based on those models are the ones of Fan et al. (1999) and Alves et al. (2001), which fully agree

with each other and where a maximum Deborah number value of around $De \approx 1$ was found for steady state numerical solutions. Keeping attention focused on dilute or semi-dilute polymer solutions, the next step in terms of complexity of molecular-based rheological modeling is to introduce finite dumbbell extensibility and evolve from the Oldroyd-B to the FENE-type models (Bird et al., 1987). The expectation here is that by introducing more realism into the physical representation of the polymer molecular behaviour, at the same time the numerical solution difficulties will be softened and higher values of Deborah number can be attained. Since we also want to separate elastic effects from those due to shear thinning in viscosity, we first consider the FENE-type equation proposed by Chilcott and Rallison (1988) known as the FENE-CR model.

2. Governing equations

The constitutive model is composed by an evolution equation for the configuration tensor:

$$\lambda \overset{\triangledown}{A} = -f(A)(A - I) \tag{1}$$

from which the extra stress tensor can be explicitly expressed by means of a Giesekus expression:

$$\tau = \frac{\eta_p f(A)}{\lambda}(A - I) \tag{2}$$

Equations (1) and (2) comprise the so-called FENE-CR model which although derived from empirical considerations (as noted by Bird and Wiest, 1995; the empiricisms are of the same level as those invoked for the well-known Peterlin approximation in the FENE-P model), tend to provide a much better representation of the material functions of a Boger fluid, especially regarding the shear-thinning of the normal stress coefficient. The stretch function $f(A)$ in Eq. (1) depends on the extensibility parameter L^2, which represents the ratio of the maximum to equilibrium average dumbbell extensions, and is given by:

$$f(A) = \frac{1}{1 - Tr(A)/L^2} \tag{3}$$

This is the same function of the FENE-P model (referred to as Z in the original paper, Bird et al. 1980) and it is derived by recalling the Peterlin's approximation ($\langle f(QQ) \rangle \approx f(\langle QQ \rangle)$ where $A = \langle QQ \rangle$; Q is the end-to-end vector).

For a matter of computational convenience, and indeed to spare memory resources, it may be advantageous to substitute the stress tensor for the conformation tensor in Eqs. (1) and (2), giving:

$$\tau + \lambda \frac{D}{Dt}(\frac{\tau}{f}) = \eta_p(\nabla u + \nabla u^T) + \frac{\lambda}{f}(\tau \cdot \nabla u + \nabla u^T \cdot \tau) \tag{4}$$

and: $\quad f(\tau) = \dfrac{L^2 + (\lambda/\eta_p)Tr(\tau)}{L^2 - 3} \tag{5}$

Equation (4) is the FENE-CR constitutive equation, to be solved in conjunction with the equation of motion:

$$\rho \frac{Du}{Dt} = -\nabla p + \eta_s \nabla \cdot (\nabla u + \nabla u^T) + \nabla \cdot \tau \tag{6}$$

and the incompressibility constraint:

$$\nabla \cdot u = 0 \tag{7}$$

In these equations, λ is the relaxation time, p is the pressure, ρ is the fluid density, and the solvent stress was assumed to follow a Newtonian relationship. An additional simplification which allows existing numerical methods to be used with minor modifications for solving Eq. (4) is to discard the variation of $D(1/f)/Dt$ and write:

$$\tau + \frac{\lambda}{f} \frac{D}{Dt}(\tau) = \eta_p(\nabla u + \nabla u^T) + \frac{\lambda}{f}(\tau \cdot \nabla u + \nabla u^T \cdot \tau) \tag{8}$$

This represents a modified FENE-CR model (designated by FENE-MCR), first used by Coates et al. (1992) and later by a number of other authors in different studies, which included the present flow configuration. It should be stressed that the steady-state rheometrical functions of FENE-CR and FENE-MCR coincide, hence not much differences should occur in steady-state complex flows as the effect of $\boldsymbol{u} \cdot \nabla (1/f)$ can be important only in strong convective regions in a flow. This conclusion will be demonstrated with the present numerical results for the flow around a cylinder. It is also important to refer at this point that a number of other authors have simulated the flow of the FENE-MCR fluid around a confined cylinder and in this sense precise benchmark solutions are in order.

It is interesting to notice that Eq. (4) can be written in terms of an effective relaxation time under a fully conservative form:

$$\boldsymbol{\tau} + \frac{D}{Dt}(\lambda_{ef}\boldsymbol{\tau}) = \eta_p(\nabla\boldsymbol{u} + \nabla\boldsymbol{u}^T) + (\lambda_{ef}\boldsymbol{\tau} \cdot \nabla\boldsymbol{u} + \nabla\boldsymbol{u}^T \cdot \lambda_{ef}\boldsymbol{\tau}) \qquad (9)$$

where $\lambda_{ef} \equiv \lambda_{ef}(\tau) = \lambda/f(\tau)$ varies as a function of the first invariant of the stress field. Hence, from a numerical point of view, this model is more satisfying as it allows a consistent conservative formulation for the convection fluxes.

3. Discretisation and solution procedure

A fully implicit, sequential (decoupled) algorithm is employed to solve the set of differential governing equations given in the previous section, which must first be transformed into algebraic equations by means of a finite volume discretisation on a collocated, non-orthogonal mesh. Both the spatial discretisation, which employs the CUBISTA scheme of Alves et al. (2003), and the temporal discretisation, with a three time level representation of the unsteady terms in the equations, are formally second order accurate. The algorithm was explained in detail in Oliveira (2001) and only an outline is given here.

The discretised constitutive equation for any cell P is:

$$a_P^\tau \boldsymbol{\tau}_P^{(n+1)} = \sum_F a_F^\tau \boldsymbol{\tau}_F^{(n+1)} + S_\tau(\nabla\boldsymbol{u}^*) + S_\tau^{HOS} + \frac{\lambda_{ef}V}{\delta t}\left(2.0\boldsymbol{\tau}_P^{(n)} - 0.5\boldsymbol{\tau}_P^{(n-1)}\right) \qquad (10)$$

with: $a_P^\tau = \left(1.5\dfrac{\lambda_{ef}V}{\delta t} + V + \sum_F a_F^\tau\right)$; $\lambda_{ef} = \lambda/f(\tau_P^*)$,

and where the stress coefficients a_F^τ are composed by convective fluxes. These are evaluated at the cell faces located between cell P and any of its neighbouring cells F (summations are over 4 neighbours, in a 2D problem). The stress source terms comprise a part of the upper-convected derivative proportional to velocity gradients $\nabla\boldsymbol{u}$, and a deferred correction part related to the high-resolution scheme CUBISTA. In Eq. (10), V is the volume of a cell and the factors 1.5, 2.0 and 0.5 arise from application of the three time level scheme to represent the unsteady term $\partial\boldsymbol{\tau}/\partial t$ (different levels of time are denoted by superscripts (n) and * denotes existing, or previous iteration, values).

The discretised momentum equation is:

$$a_P\boldsymbol{u}_P^{**} = \sum_F a_F\boldsymbol{u}_F^{**} - \nabla p^* + S_u(\nabla\cdot\boldsymbol{\tau}^{(n+1)}) + S_u^{HOS} + \frac{\rho V}{\delta t}\left(2.0\boldsymbol{u}_P^{(n)} - 0.5\boldsymbol{u}_P^{(n-1)}\right) \qquad (11)$$

with: $a_P = \left(1.5\dfrac{\rho V}{\delta t} + \sum_F a_F\right)$

and where the coefficients a_F have now both convective and diffusive contributions. In general, the velocity field $\boldsymbol{u}^{**}$ obtained from implicit solution of Eq. (11) will not satisfy the discretised continuity equation:

$$\nabla\cdot\boldsymbol{u}^{(n+1)} = 0 \qquad (12)$$

and for that reason $\boldsymbol{u}^*$ and the intermediate pressure p^* need to be corrected by $\boldsymbol{u}' = \boldsymbol{u}^{(n+1)} - \boldsymbol{u}^{**}$ and $p' = p^{(n+1)} - p^*$. The corrected velocity field is determined from a factored form of the momentum equation:

$$1.5\frac{\rho V}{\delta t}\boldsymbol{u}_P^{(n+1)} + \left(\sum_F a_F\right)\boldsymbol{u}_P^{**} = \sum_F a_F\boldsymbol{u}_F^{**} - \nabla p^{(n+1)} + S_u(\nabla\cdot\boldsymbol{\tau}^{(n+1)}) + S_u^{HOS} + \frac{\rho V}{\delta t}\left(2.0\boldsymbol{u}_P^{(n)} - 0.5\boldsymbol{u}_P^{(n-1)}\right) \qquad (13)$$

where, by comparison with Eq. (11), we see that only the inertial and the pressure gradient terms have been updated to a new time level (n+1) stage. A Poisson-like pressure correction equation is derived by subtracting Eq. (11) from Eq. (13) and imposing the divergence-free constraint, Eq. (12), to yield.

$$a_P^p p_P^{'} = \sum_F a_F^p p_F^{'} - (\nabla \cdot \boldsymbol{u}^{**}) \qquad (14)$$

with: $a_P^p = \sum_F a_F^p$.

So we see that all linearised sets of algebraic equations to be solved can be cast under the standard form:

$$a_P \phi_P = \sum_F a_F \phi_F + b \qquad (15)$$

with the summation for index F being over the 4 cell neighbours of cell P, in a 2D application, or over the 6 cell neighbours in 3D applications. These large systems of equations are solved with iterative solvers: the conjugate gradient method preconditioned with an incomplete LU decomposition, for the case of the symmetric $p^{'}$ equation; and the bi-conjugate gradient method for the other variables (velocity and stress components). There are two levels of iteration in the algorithm. The iterations inside the solvers, the "inner" iterations, are pursued until the initial residuals on entering the solver decay by two orders of magnitude. The "outer" iterations, inside a time step δt, arise because: (i) $S_\tau(\nabla \boldsymbol{u})$ in the stress equation, Eq. (10), depends on the velocity field, and $S_u(\nabla \cdot \boldsymbol{\tau})$ in the velocity equation, Eq. (11), depends on the stress field; (ii) the factored momentum equation, Eq. (13), devised to deal with the linear velocity/pressure coupling is only approximate; (iii) explicit non-linearities are present in the convection terms of the momentum equation and the $f(\tau)$ function in the stress equation. These outer iterations are repeated through Eqs. (10) to (14) until $\boldsymbol{\tau}^{(n+1)}$, $\boldsymbol{u}^{(n+1)}$ and $p^{(n+1)}$ do not change; in practice this is achieved by controlling the normalized residuals of the equations (in terms of the L_1 norm) which are required to be below a tolerance of 10^{-4}.

4. Results

In this paper we consider only the problem of the flow around the bounded cylinder placed symmetrically in a plane channel. In the next paragraphs we discuss issues related to boundary conditions, numerical accuracy and computational meshes, the prediction of the drag coefficient as a function of elasticity level, and the occurrence of an unsteady flow regime.

Table 1. Some characteristics of the computational meshes.

Mesh	dimension	domain	NC	NS	δr min	δs min	δs min wake
M45	2D	half	9918	152	0.00646	0.0207	0.0207
M30WR	2D	half	5310	115	0.00962	0.0314	0.01
M60WR	2D	half	21240	230	0.00962	0.0314	0.01
M30WR	2D	full	10620	230	0.00962	0.0314	0.01
M30WR-O	2D	Full/odd	11040	237	0.00962	0.0314	0.01

NC- total Number of Cells; NS-number of cell on cylinder surface; δr, δs minimum cell spacing (norm. by R)

Table 2. Predicted drag coefficient on mesh M45 (Re=0; FENE-MCR; L=12).

De	0	0.5	1.0	1.5	2.0	2.5	3.0	4.0	5.0	6.0	7.0	8.0	10.0
C_D	132.5	119.8	118.04	118.76	119.35	119.68	119.85	119.97	119.96	119.88	119.78	119.66	119.39

For the bounded flow with a cylinder-to-channel ratio of $B \equiv R/H = 0.5$ we have first done computations with the mesh M45 of our previous work (Alves et al 2001) which was a medium mesh for the UCM model. Due to shear thinning in the relaxation time, the FENE-CR model poses much less burden upon the numerical method and that mesh is quite adequate to resolve and capture with accuracy the features of the flow around the cylinder except the normal stress variation along the downstream stress wake. This is a very thin flow feature and proper resolution requires refinement along the θ-direction for $\theta = 180^0$ (i.e. clustering the mesh around the line $y = 0$, $x > 0$).

Some of the main characteristics of the various meshes are given in Table 1, including the total number of control volumes (or cells, NC), the number of control volumes around the surface of the cylinder NS, the number of cells

placed radially from the cylinder to the channel wall NR (this is the figure given after the M indication), and the minimum cell spacing normalized with the cylinder radius along the radial, δr, and the azimuthal θ directions, δs. Mesh M30 has less cells along the radial distance compared with mesh M45, but it is more refined along the wake; for this reason the qualification WR (for wake-refined) is added to the mesh designation. Figure 2 shows a detail of the mesh M30WR-O, with an odd number of control volumes on the downstream side of the cylinder.
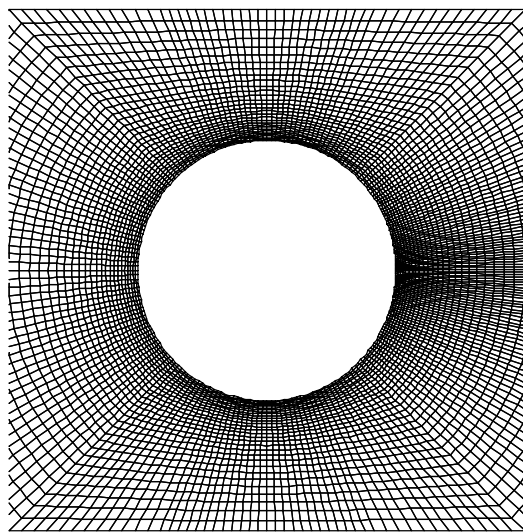
Figure 2 – Zoomed view ($x \in [-2H, +2H]$, $y \in [-2H, +2H]$) of mesh M30WR-O: blockage ratio $B = 0.5$, full cylinder with wake-refined mesh, odd number of cells on back of cylinder.

For the half-domain meshes, symmetry is assumed about the longitudinal axis ($y = 0$) and therefore the boundary conditions are:

(i)   Inlet ($x = -L_1 = -20H$): Dirichlet conditions based on analytical profiles for fully developed Poiseuille flow in planar channel.

(ii)   Outlet ($x = +L_2 = +60H$): Neumann conditions for all dependent variables, including the axial pressure gradient $\partial p / \partial x = 0$.

(iii)   Solid walls (channel wall, $y = \pm 2H$; cylinder surface, $r = R$): no slip boundary conditions.

(iv)   Symmetry plane ($y = 0$): symmetry conditions, that is zero normal gradients for all variables and zero normal velocity components. This boundary condition is not needed for full domain meshes.
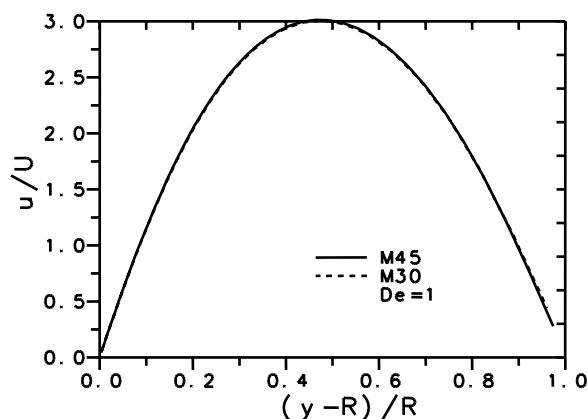

Figure 3 – Lateral profile of the u-velocity component in the narrow gap ($x = 0$) – effect of mesh refinement at $De = 1$.
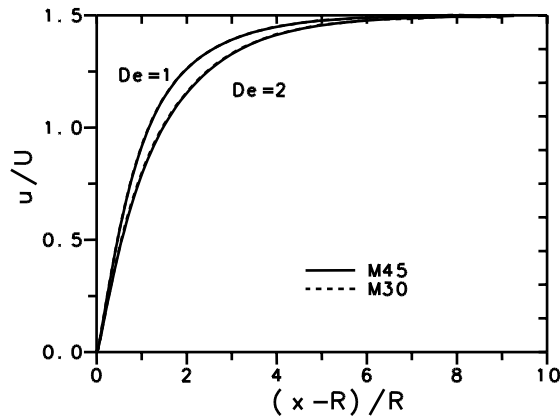
Figure 4 – Mesh refinement: velocity distribution along the cylinder wake ($y = 0$) at $De = 1$ and 2.
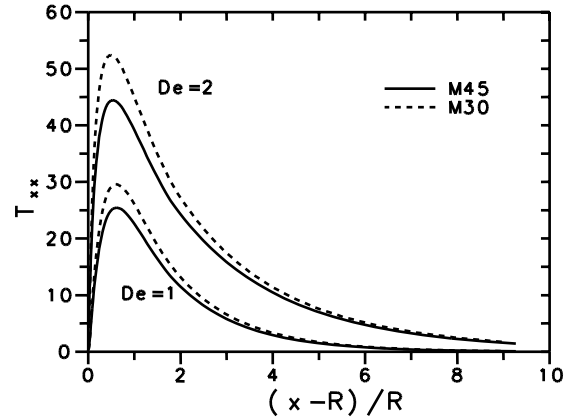

Figure 5 – Mesh refinement: normal stress distribution along the cylinder wake ($y = 0$) at $De = 1$ and 2.

Results for the mesh refinement study are presented in Fig. 3, where the u -velocity profiles are given along the transversal direction y in the narrow gap between cylinder and channel wall, and Figs. 4 and 5, where the longitudinal variations of axial velocity and normal stress τ_{xx} components along the centerline are shown. These predictions were obtained on the two consistently refined meshes for the half-domain, M45 and M30WR of Table 1, and for Deborah numbers of 1 and 2. It is clear that good agreement between results from the different meshes is achieved for all quantities except the normal stress in the birefringence strand, thus indicating adequate resolution provided by the meshes used in this study. In terms of the drag coefficient C_D obtained from integration of the full stress tensor around the cylinder surface, differences in results on the various meshes are undistinguishable in a graph and the corresponding variation with elasticity will be discussed below. The only quantity sensitive to azimuthal mesh refinement is τ_{xx} but, clearly, its exact prediction does not affect either C_D or the distribution of the other dependent variables (velocity; stress). As shown in Fig. 6, the τ_{xx} versus x variation along the line $y = 0$ can be more accurately predicted by carrying out computations on a wake-refined mesh (as in Alves et al. 2001) or by employing a mesh with odd-spaced control volumes at the back of the cylinder, with a row of cells placed exactly along the "symmetry" line $y = 0$. In this case the dependent variables are calculated at positions (control volume centers) placed exactly along the downstream midline in a full-domain mesh, without relying on interpolation, and hence the sensitivity of the τ_{xx} prediction on mesh refinement is highly alleviated. Notice from Fig. 6 how mesh M30WR-O with just 11040 cells gives almost the same predictions as mesh M60WR which would have 2x21240=42480 cells for the full domain.
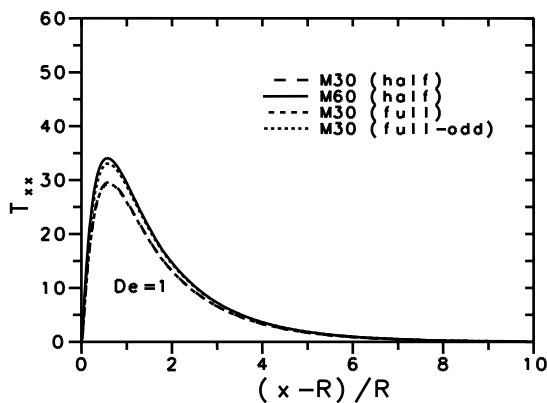

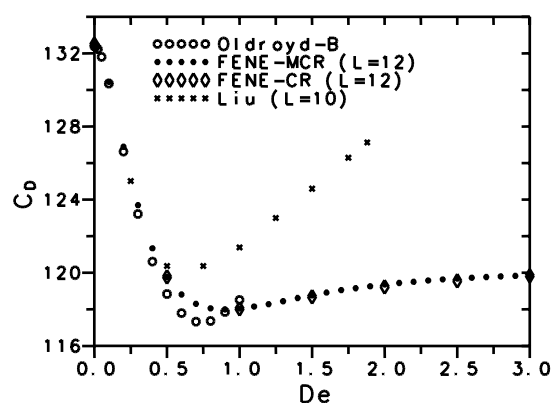Figure 6 – Effect of mesh distribution on the normal stress profile along the centreline ($y = 0$) at De=1.

Figure 7- Variation of the drag coefficient C_D with the Deborah number De (FENE-MCR $L = 12$) and comparison with predictions for the Oldroyd-B [Alves et al] and Fene-CR ($L = 10$) [Liu] models.

A convenient measure of the quality of the numerical predictions is provided by the drag coefficient obtained by integrating the total (solvent plus polymeric) stress and pressure contributions over the cylinder surface. This constitutes therefore a global solution functional, evaluated as:

$$C_D = \frac{1}{\eta_0 U} \int_{cyl} \left(-p\boldsymbol{I} + \boldsymbol{\tau} + \eta_s (\nabla\boldsymbol{u} + \nabla\boldsymbol{u}^T) \right) \bullet \boldsymbol{n} \bullet \boldsymbol{x} dA \qquad (16)$$

and representing the longitudinal component of the force exerted by the fluid upon the cylinder, normalized by a diffusive force scale appropriate to the inertialess conditions under consideration. The predicted variation of C_D with elasticity is shown in Fig. 7 (and Table 2), for an extensibility parameter $L^2 = 144$, where it is compared with predictions for the Oldroyd-B fluid obtained by Alves et al. (2001) and for the FENE-CR at a slightly different $L^2 = 100$ by Liu et al. (1998). For $De \geq 0.5$, the predictions of Liu et al. start deviating from the trend established by the current simulations, an effect that cannot be explained by the somewhat different extensibility parameter ($L = 10$, instead of 12). In order to check this point we have carried out additional simulations for $L = 10$ and the corresponding C_D versus De predictions, not shown in the figure, lie slightly below our predictions with $L = 12$, so being even further away from Liu's numerical data. For the Oldroyd-B fluid, both the works of Fan et al. (1999) and Alves et al. (2001) showed signs of numerical divergence or unrealistic wiggles in the τ_{xx} variation behind the cylinder for $De > 1.0$ and therefore no steady-state solutions could be obtained for that higher Deborah number range. There was, however, a remarkable agreement between the C_D predictions of those authors in the range $0 \leq De \leq 1$, giving confidence on the correctness of their results, a view further corroborated by the fact that different numerical methods were utilized (finite elements by Fan et al., and finite volumes by Alves et al.).

Figure 7 shows a higher rate of decay of C_D with De, in the range $0.5 \leq De \leq 1.0$, for the infinite extensibility Oldroyd-B fluid compared with the FENE-MCR at $L^2 = 144$, and suggests a stronger drag increase at higher elasticity, where results could not be obtained, either because of numerical problems or because the flow eventually becomes unsteady or three dimensional. That figure is also important to demonstrate that the solution obtained with the exact FENE-CR model essentially follows the solution with the modified model, at least for the steady state conditions under consideration.
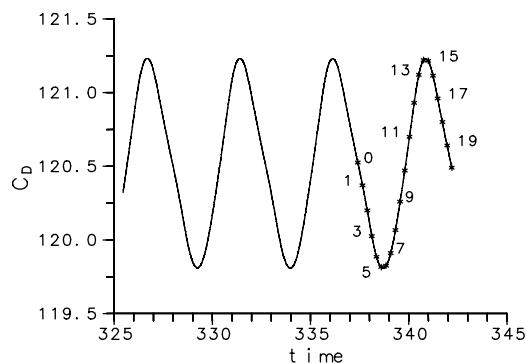

Figure 8 – Time dependent evolution of the drag coefficient at $De = 1.5$ (FENE-MCR, $L = 12$, mesh M30WR-O).

The drag results of Fig. 7 were obtained with the mesh M30 WR (wake-refined) of Table 1, which was deployed over only half of the flow domain ($y \geq 0$) by assuming symmetry about the centerline $y = 0$. For the full domain, the C_D values of that figure need not be multiplied by a factor of 2, but otherwise no discernable differences can be seen in a graph amongst predictions on the half and the full domain meshes, and indeed with the more refined meshes M60 WR. However, for $De > 1.3$ steady state calculations on the full domain meshes cannot be converged to arbitrary low stopping tolerances (we recall that our method is iterative and some convergence criterion must be met); the residuals of the algebraic equations stagnate at a certain value and start fluctuating around that level. If the calculations are then pursued by tracking the solution accurately in time (with the second-order method described in Section 3), it is possible to observe that a definite time-varying regime sets in, basically confined to a small region in the near wake of the cylinder ($1 \leq x \leq 1.2, y \leq \pm 0.2$), while in the rest of the domain the flow remains unvarying and steady. Since the drag coefficient is a particularly sensitive parameter to possible time-varying events occurring on the back of the cylinder (such as separation and localized recirculation), the above observations can be substantiated by tracking C_D in time as in the plot of Fig. 8. A perfectly sinusoidal variation of C_D versus time is observed, with a period of $\approx 4.7 R/U$.
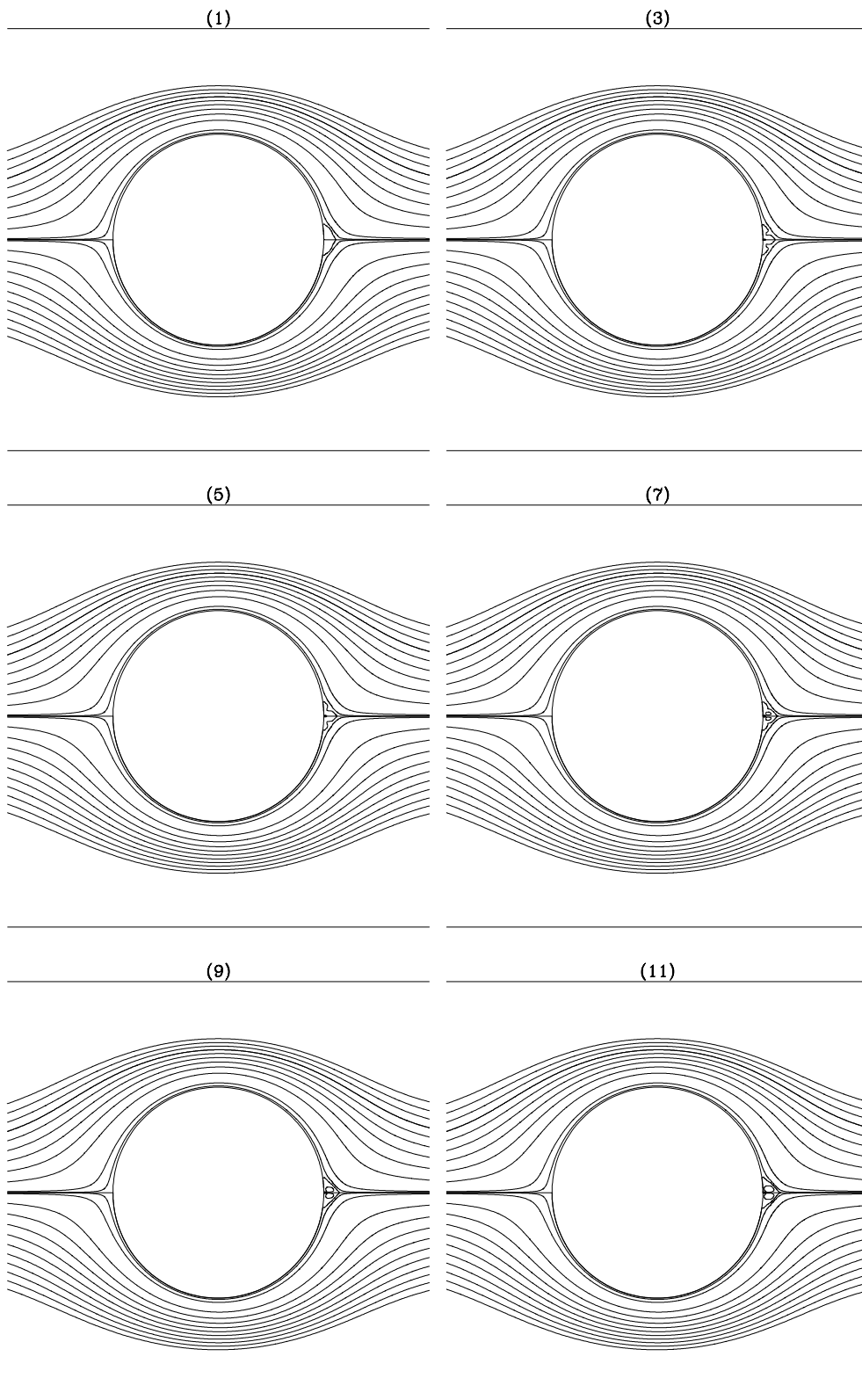
(1)

(3)

(5)

(7)

(9)

(11)

Figure 9 – Instantaneous streamline plots at equally spaced instants in time during a period, for $De = 1.5$ (continued).

(13)   (15)

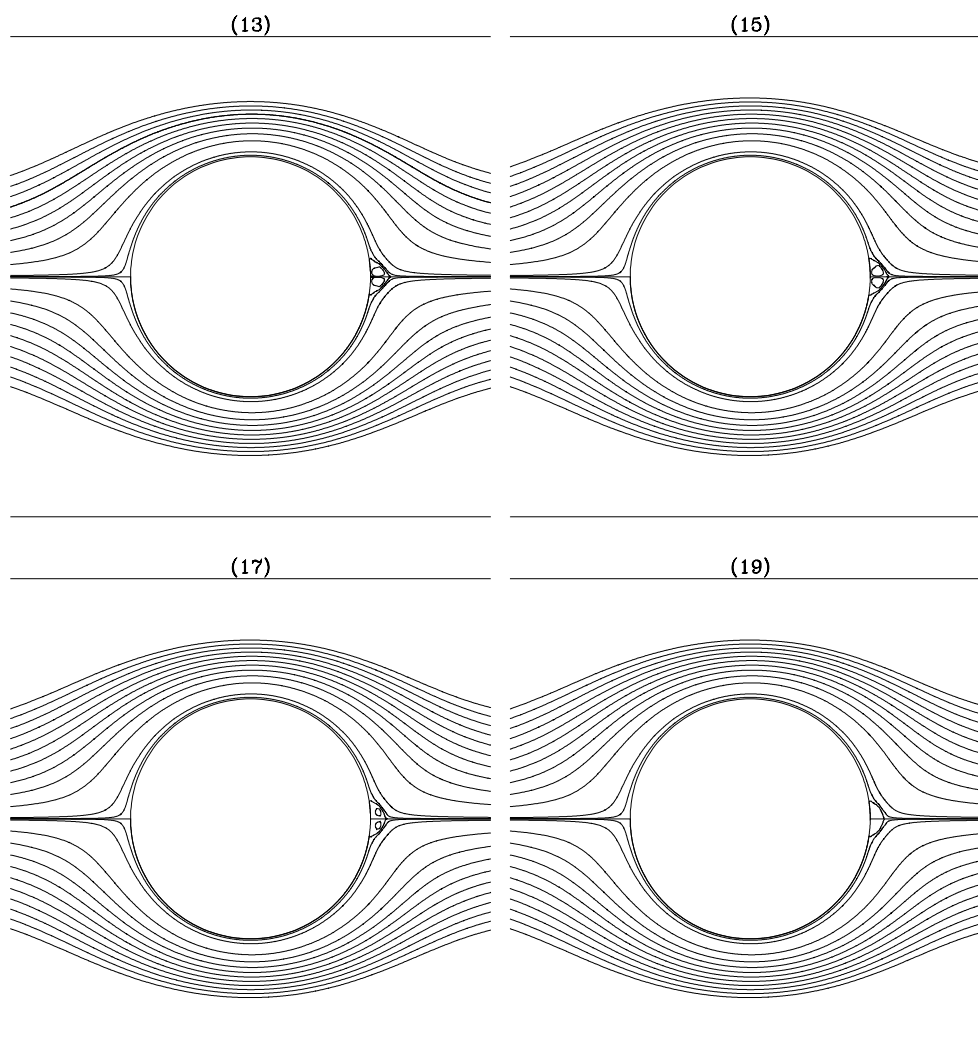(17)   (19)

Figure 9 – Instantaneous streamline plots at equally spaced instants in time during a period, for $De = 1.5$ (continuation).

In order to explain the periodic variation of C_D we have considered 20 equally spaced instants in time within a period, which are marked in Fig. 8 and will be denoted by numbers from 1 to 20, and observed the corresponding instantaneous streamlines plots. These are shown in Fig. 9 for every other instant in time, the number on top of each plot; along the main flow direction, from left to right, 21 streamlines are shown having equally spaced normalized stream-function values ranging from $\psi = 0$ to ± 1 (with intervals of 0.1) and, in addition, 4 other streamlines are shown very close to the centerline, with $\psi = \pm 0.01$ and ± 0.001. The key flow feature observed in Fig. 9 is the formation of a very small recirculation zone attached to the rear of the cylinder, which pulsates in time: it gradually becomes filled with the viscoleastic fluid, followed by a gradual decrease in size while the fluid partly leaves the bubble. When the bubble attains its minimum size and recirculation strength, at time instant 5, the drag coefficient is also at a minimum; similarly, when the bubble attains its maximum size, at instants $\approx 14-15$, C_D is at a maximum. It is noted that the bubble remains symmetric about the x-axis during the whole pulsating period, but the dynamic process leading to its formation can only be resolved by simulations with the full flow domain, without relying on symmetry.

It is relevant to mention that the size of the time step (δt) used in the computations is automatically adjusted in order to guarantee convergence of the iterations inside a time step cycle. We have started with a value of $\delta t = 0.01$ (normalized with R/U), typical for this type of computations (e.g. Oliveira, 2001), but as the simulation proceeded that was successively decreased until a value of $\delta t = 2.3915 \times 10^{-3}$ was reached. This time step then remained constant during the computations of the periodic flow represented in Fig. 8. The streamlines plots of Fig. 9 are separated by a time interval corresponding to 100 such time steps (200 for the odd time intervals shown).

In their experiments with a PIB polymer solution in the same geometry (blockage $B = 0.5$), McKinley et al. (1993) observed a transition to a periodic time dependent flow at $De(\gamma) \approx 1.85$, but that regime was preceded by a first transition from a steady 2D to a steady 3D flow at a lower $De(\gamma) \approx 1.3$. This steady three-dimensional flow

corresponded to the formation of a wake cellular structure, with zones of high and low axial velocities in the wake repeated every characteristic wavelength along the spanwise, neutral direction (here taken as z). Obviously, 3D simulations are required to capture this cellular structure but the few attempts we have taken towards that goal have been unsuccessful (these are not reported here for a matter of space). Future attempts will have to consider cyclic boundary conditions on the end planes along the z-direction in order to have adequate spanwise mesh resolution but still keeping the total number of control volumes (and degrees of freedom) within the limits imposed by current available computer resources. The imposition of those boundary conditions is not without difficulties as the wavelength of the cellular structure is not known apriori and that will affect the choice of the computational domain size along z. Based on the experiments of McKinley et al we may conjecture that the time-dependent 2D flow resulting from the present simulations, and represented in Fig. 9, could be the triggering mechanism leading to the formation of the 3D cellular structure in the wake (cf. the photograph in their Fig. 14 where the repeated cells are clearly visible).

5. Conclusions

Computations have been performed with a finite volume method for the inertialess flow of a viscoelastic FENE-MCR fluid around a cylinder confined in a planar channel with a blockage ratio of 0.5. Steady state results were obtained in the range $De = 0$ to 10 when the computational meshes covered only half of the flow domain with symmetry conditions assumed along the centerline. However, for the full domain and with an especially designed mesh having a row of cells along the centerline in the cylinder wake, the flow was found to be unsteady and periodic for $De > 1.3$, with the formation of a small recirculation bubble attached to the cylinder downstream "stagnation" point, which grows and decreases in a pulsating fashion in time. Due to that bubble the drag coefficient tends to increase, compared with the steady-state situation without bubble, and its magnitude varies in time following a sinusoidal curve at the particular value of $De = 1.5$. Such phenomenon for the flow at zero Reynolds number of non-Newtonian fluids possessing viscoelastic characteristics has never been reported in previous studies of flow around a cylinder.

6. References

Alves, M.A., Pinho, F.T., Oliveira, P.J., 2001, "The flow of viscoelastic fluids past a cylinder: finite-volume high-resolution methods", J. Non-Newtonian Fluid Mech., Vol. 97, pp. 207-232.

Alves, M.A., Oliveira, P.J., Pinho, F.T., 2003, "A convergent and universally bounded interpolation scheme for the treatment of advection", Int. J. Numer. Meth. Fluids , Vol. 41, pp. 47-75.

Bird, R.B., Hassager, O., Armstrong, R.C., Curtiss, C.F., 1987, "Dynamics of Polymeric Liquids, Vol 2: Kinetic Theory", John Wiley, New York.

Bird, R.B., Dotson, P.J., Johnson, N.L., 1980, "Polymer solution rheology based on a finitely extensible bead-spring chain model", J. Non-Newtonian Fluid Mech., Vol. 7, pp. 213-235.

Bird, R.B., Wiest, J.M., 1995, "Constitutive equations for polymeric liquids", Annual Rev. Fluid Mech. 27,pp. 169-193.

Brown, R.A., McKinley, G.H., 1994, J. Non-Newtonian Fluid Mech. Vol. 52, pp. 407-413.

Chilcott, M.D., Rallison, J.M., 1988, "Creeping flow of dilute polymer solutions past cylinders and spheres", J. Non-Newtonian Fluid Mech., Vol. 29, pp. 381-432.

Coates, P.J., Armstrong, R.C., Brown, R.A., 1992, "Calculation of steady-state viscoelastic flow through axisymmetric contractions with the EEME formulation", J. Non-Newtonian Fluid Mech., Vol. 42, pp. 141-188.

Dou, H-S., Phan-Thien, N., 1999, "The flow of an Oldroyd-B fluid past a cylinder ina channel: adaptive viscosity vorticity (DAVSS-Ω) formulation", J. Non-Newtonian Fluid Mech., Vol. 87, pp. 47-73

Fan, Y., Tanner, R.I., Phan-Thien, N., 1999, "Galerkin/least-squere finite-element methods for steady viscoelastic flows", J. Non-Newtonian Fluid Mech., Vol. 84, pp.233-256

Liu, A.W., Bornside, D.E., Armstrong, R.C., Brown, R.A., 1998, "Viscoelastic flow of polymer solutions around a periodic, linear array of cylinders: comparisons of predictions for microstruture and flow fields", J. Non-Newtonian Fluid Mech., Vol. 77, pp. 153-190.

McKinley, G.H., Armstrong, R.C., Brown, R.A., 1993, "The wake instability in viscoelastic flow past confined circular cylinders", Phil. Trans. R. Soc. Lond. A , Vol. 344, pp. 265-304.

Oliveira, P.J., 2001, "Method for time-dependent simulations of viscoelastic flows: vortex shedding behind cylinder", J. Non-Newtonian Fluid Mech. Vol. 101, pp. 113-137.

Sun, J., Smith, M.D., Armstrong, R.C., Brown, R.A., 1999, "Finite element method for viscoelastic flows based on the discrete adaptive viscoelastic stress splitting and the discontinuous Galerkin method: DAVSS-G/DG", J. Non-Newtonian Fluid Mech., Vol. 86, pp. 281-307.

7. Copyright Notice